Supplementary Information

Prussian blue coupling with zinc oxide as a protective layer:

An efficient cathode for high-rate sodium-ion batteries

Yun Qiao, Gangya Wei, Jiabao Cui, Mingming Zhang, Xiaoguang Cheng, Dandan He, Shuan Li and Yang Liu[*]

School of Chemistry and Chemical Engineering, Key Laboratory of Green Chemical Media and Reactions, Ministry of Education, Henan Normal University. Xinxiang, Henan 453007, China

E-mail: liuy986@htu.edu.cn, qyvec@163.com.

Experimental section

Synthesis of Prussian blue (PB: Na$_x$FeFe(CN)$_6$): PB was obtained by the typical method of co-precipitation. 1.94 g sodium ferrocyanide decahydrate (Na$_4$Fe(CN)$_6$·10H$_2$O) and 1.66 g Iron(II) sulfate heptahydrate (FeSO$_4$·7H$_2$O) were respectively dissolved into 200 mL deionized water. Then, 15.00 g sodium citrate (Na$_3$C$_6$H$_5$O$_7$·2H$_2$O) was added to the FeSO$_4$·7H$_2$O solution. Finally, the above two precursor solutions were mixed and maintained at room temperature for 6 h. Finally, the cubic Na$_x$FeFe(CN)$_6$ was obtained after centrifuging, washing with deionized water and ethanol followed by drying at 80 °C for 12 h.

Synthesis of PB@ZnO composite: The as-obtained cubic Na$_x$FeFe(CN)$_6$ (0.20 g) were added into the 100 mL deionized water and 100 mL ethanol under magnetic stirring. Zinc acetate (0.02 g) and sodium bicarbonate (0.02 g) were added to the above solution. The mixed solution was heated at 80 °C until all the solvents are removed. Then, the precursor mixtures were heat treated in tubular furnace at 200 °C for 3 h under N$_2$ atmosphere. The final PB@ZnO composite was successively washed with deionized water and ethanol for three times, dried at 80 °C for 12 h. For comparison, ZnO was also prepared under the same procedure mentioned above without adding PB.

Characterization: The structure and phase of the products were collected by X-ray diffraction (XRD, D8 Advance, Bruker) equipped with Cu Kα1 radiation. The morphology was carried on field-emission scanning electronic microscopy (FE-SEM; JSM-6700F) and transmission electron microscopy (TEM, JEOL JEM-2100). X-ray photoelectron spectroscopy (XPS) was measured on a VG MultiLab 2000 system with a monochromatic Al Kα X-ray source. All the spectra were calibrated by C 1s (284.6 eV). Thermogravimetric analysis (TGA) and differential scanning calorimetry (DSC) were conducted on Netzsch STA449F3 analyzer from 50 to 600 °C at a rate of 10 °C min^{-1} in flowing air. Fourier transform infrared spectra (FTIR) were collected at a NEXUS spectrophotometer.

Electrochemical measurements: Electrochemical performance was evaluated on

CR2025 coin cells. The electrodes were manufactured by mixing 70 wt. % active materials, 20 wt. % Super P and 10 wt. % sodium alginate, coating onto an aluminum foil and subsequent drying at 80 °C for 12 h under vacuum. The coin cells were assembled in an argon-filled glove box (H_2O, O_2 < 0.1 ppm), The counter electrode, separator, and electrolyte are sodium metal, Whatman (GF/D) glass fiber, 1 mol L^{-1} $NaClO_4$ in propylene carbonate (PC) and ethylene carbonate (EC) (v/v=1:1) with 5 vol % nonreactive fluoroethylene carbonate (FEC) additives. The charge/discharge tests were conducted on a Land CT2001A testing system (Wuhan, China) within a voltage window of 2.0–4.2 V. Cyclic voltammetry (CV) measurements were performed on a CHI760E electrochemical workstation and conducted in the range of 2.0–4.2 V at a scan rate of 0.2 mV s^{-1}.
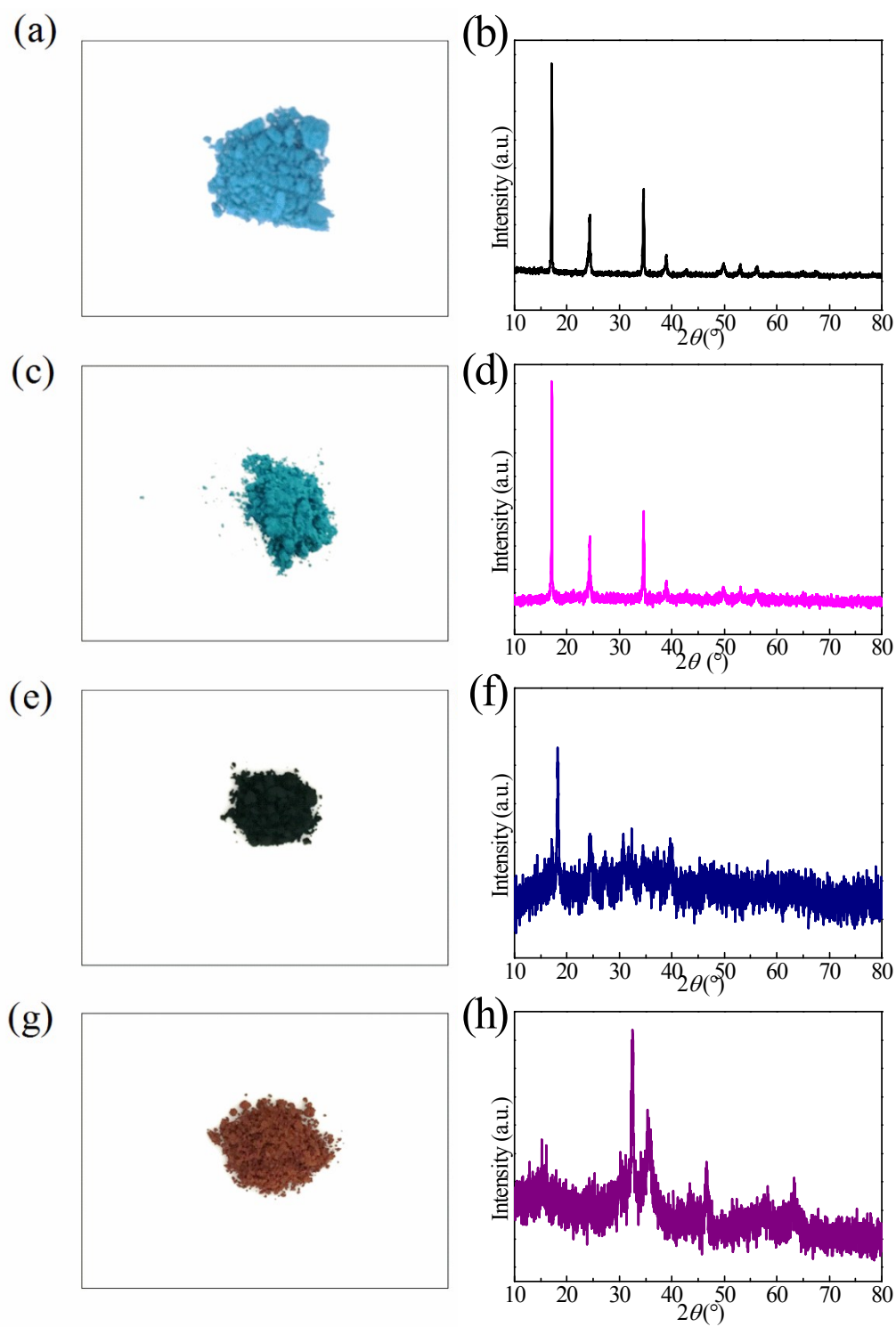
Figure S1. Digital photographs and the corresponding XRD patterns of the PB samples after heat treatment at (a, b) 150 $^{\circ}$C, (c, d) 200 $^{\circ}$C, (e, f) 250 $^{\circ}$C, (g, h) 300 $^{\circ}$C, respectively.
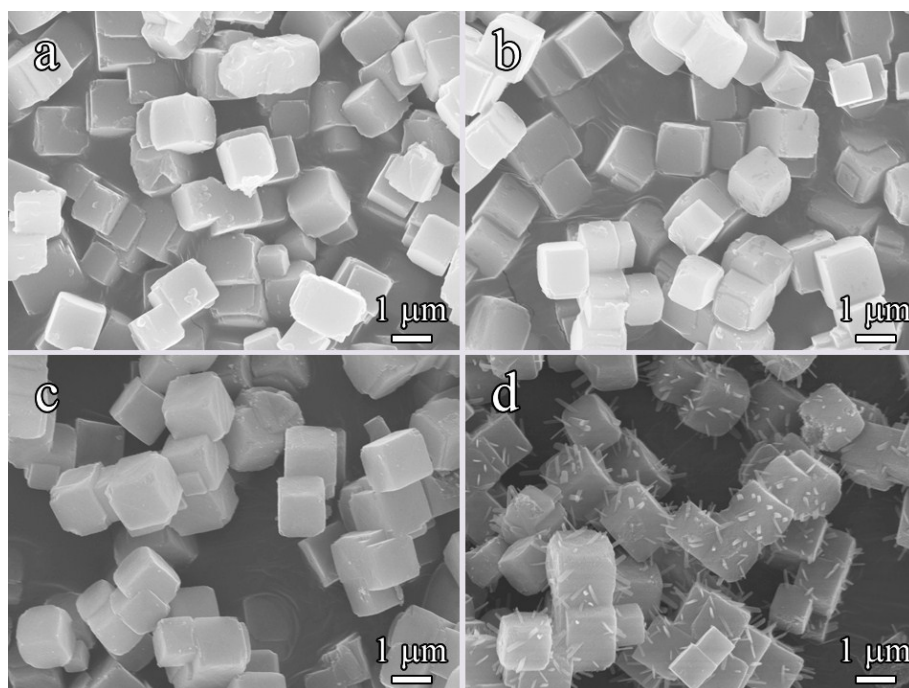
Figure S2. FE-SEM images of the PB samples after heat treatment at (a) 150 °C, (b) 200 °C, (c) 250 °C, and (d) 300 °C, respectively.
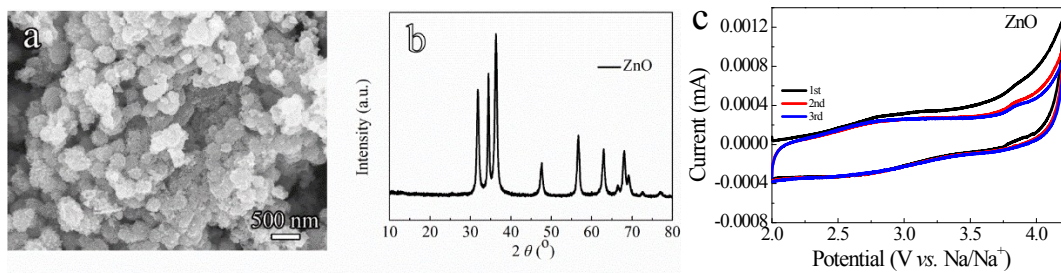
Figure S3. (a) FE-SEM image, (b) XRD pattern of as-synthesized ZnO, and (c) CV curves of ZnO as electrode from 2.0 to 4.2 V at a scan rate of 0.2 mV s^{-1}.
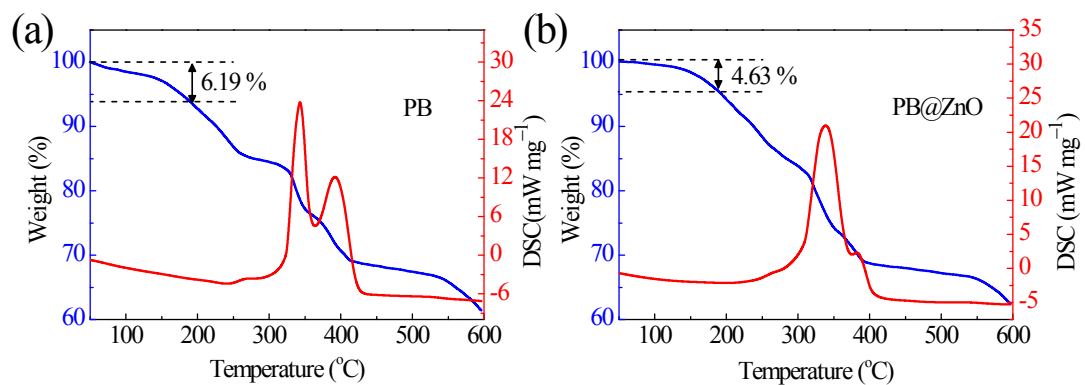
Figure S4. TG-DSC curves of the PB and PB@ZnO from 50 to 600 °C at a rate of 10 °C min^{-1} in flowing air.
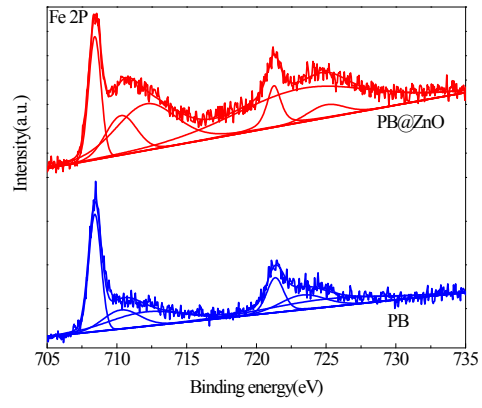
Figure S5. High-resolution spectra of Fe 2p for PB@ZnO and PB.
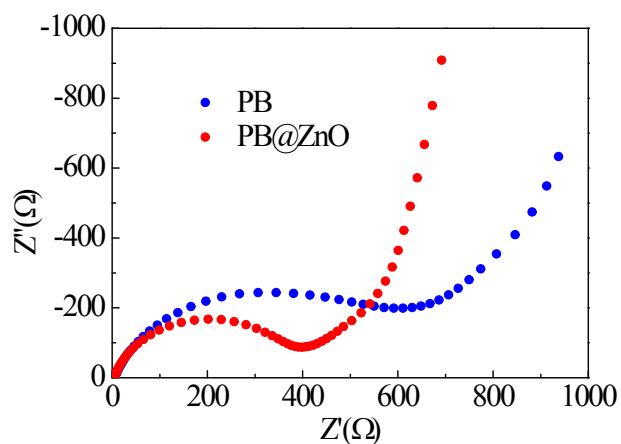
Figure S6. Electrochemical impedance spectra of the electrodes after fist cycle in the frequency range of 100 kHz–0.01 Hz.

In order to further understand the improved electrochemical performance, we performed the electrochemical impedance spectroscopy (EIS). In our case, the semicircle diameter in high-medium frequencies for PB@ZnO cathode is smaller than that of PB cathode, indicating its relatively lower charge transfer resistance, although the ZnO coating layer may be resistive against interfacial Na-ion transfer. We think that this is related with the interstitial water in the PB@ZnO composite structure. As reported, the remove of interstitial water from $Na_2MnFe(CN)_6 \cdot zH_2O$ could greatly improve the electrochemical performance of PB cathode (J. Am. Chem. Soc. 2015, 137, 2658-2664.). Therefore, the lower charge transfer resistance for PB@ZnO cathode could be attributed to the removable of interstitial water from PB structure in the low-temperature thermal treatment process. The specific reason still need further in-depth studies.
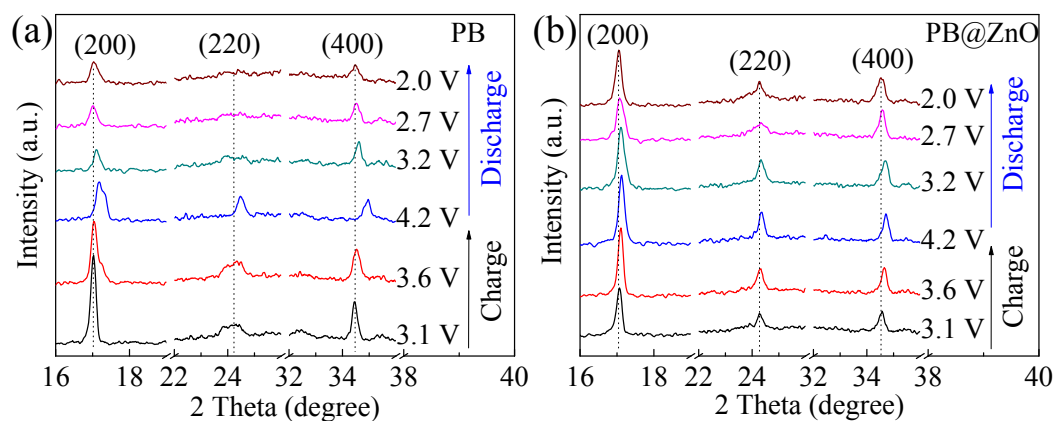
Figure S7. (a, b) *Ex situ* XRD patterns of PB and PB@ZnO cathode at different charge and discharge stage in the first cycle.

We investigated the structural evolution of PB@ZnO and PB via *ex situ* XRD at different charge and discharge stage at a current density of 0.2 A g^{-1} (Figure S7). When using PB as cathode, the diffraction peaks of (200), (220) and (400) obviously shift to high angle in the charging process (from open circuit voltage to the cut-off voltage of 4.2 V), indicating its volume shrinkage due to the extraction of Na$^+$ ions from the PB structure. Whereas, the diffraction peaks slightly shift to the low angle in the discharging process, implying the volume expansion due to the insertion of Na$^+$ ions. The structure evolution trend of PB@ZnO cathode is almost the same as that of PB. It is worth to note that, the peak shifts of PB@ZnO electrode is much smaller compared with PB cathode, indicating its unapparent volume shrinkage and expansion during the charging and discharging process. This result could be attributed to the protective coating layer of ZnO, which could prohibit PB lattice from decomposition.
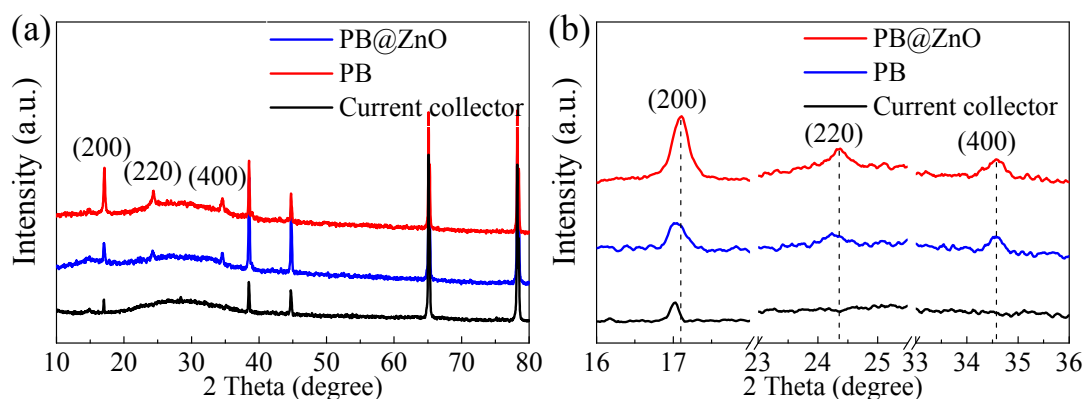
Figure S8. (a) XRD patterns of PB@ZnO and PB electrodes after charge and discharge cycling, and a blank current collector; (b) the corresponding expanded XRD patterns between 16° and 36°.

The structural information about PB@ZnO and PB electrodes were investigated by XRD after 100 cycles. As shown in Figure S8a, the XRD pattern of current collector was collected to eliminate the effect of Al foil. The (200), (220) and (400) are observed for PB@ZnO and PB in Figure S8. In order to assess the structure evolution of the electrodes in details, the expanded XRD patterns from 16° to 36° are shown in Figure S8b. Compared to the pristine electrode, the diffraction peaks of (200) and (220) for PB and PB@ZnO shift slightly to the low angle, indicating their volume expansion after long cycling due to the structural defects in PB. Notably, the shift for PB@ZnO is slighter than that of PB, meaning that the PB@ZnO could accommodate the lattice strain upon cycling because of the protective coating layer of ZnO. These results indicate that the structure of PB@ZnO cathode is stable during sodium ion extraction and insertion process.